nature catalysis

ARTICLES

https://doi.org/10.1038/s41929-017-0009-x

Metal ion cycling of Cu foil for selective C–C coupling in electrochemical CO_2 reduction

Kun Jiang[1], Robert B. Sandberg[2], Austin J. Akey[3], Xinyan Liu[2], David C. Bell[3,4], Jens K. Nørskov[2,5], Karen Chan[2,5]* and Haotian Wang[1]*

Electrocatalytic CO_2 reduction to higher-value hydrocarbons beyond C_1 products is desirable for applications in energy storage, transportation and the chemical industry. Cu catalysts have shown the potential to catalyse C–C coupling for C_{2+} products, but still suffer from low selectivity in water. Here, we use density functional theory to determine the energetics of the initial C–C coupling steps on different Cu facets in CO_2 reduction, and suggest that the Cu(100) and stepped (211) facets favour C_{2+} product formation over Cu(111). To demonstrate this, we report the tuning of facet exposure on Cu foil through the metal ion battery cycling method. Compared with the polished Cu foil, our 100-cycled Cu nanocube catalyst with exposed (100) facets presents a sixfold improvement in C_{2+} to C_1 product ratio, with a highest C_{2+} Faradaic efficiency of over 60% and H_2 below 20%, and a corresponding C_{2+} current of more than 40 mA cm^{-2}.

With the fast development of advanced technologies to efficiently harvest wind or solar energies, the cost of renewable energy in the near future is expected to decrease significantly, enabling economical conversion of carbon dioxide (CO_2) and water (H_2O) into fuels and chemicals[1–3]. The electrochemical CO_2 reduction reaction (CO_2RR) is a promising energy conversion process due to its mild reaction conditions and high energy efficiencies[4–8], but is currently challenging due to the low catalytic activity and product selectivity in aqueous solutions[9–12]. Catalysts with suitable electronic structures have been able to reduce CO_2 in water with high Faradaic efficiencies[13–24], but most of them can only catalyse two-electron reductions to carbon monoxide (CO) or formic acid (HCOOH) products, which have more facile kinetics. Further reductions to higher-value, energy-dense hydrocarbons and alcohols, and in particular C_{2+} products, is desirable for applications in energy storage, transportation and the chemical industry, but present significantly higher overpotentials[25]. This difficulty arises from the linear scaling among activation and binding energies of reaction intermediates; the catalytic surface needs to bind *CO intermediates strongly enough to build up a sufficient coverage for further reduction or C–C coupling, but the associated activation barriers also increase with stronger *CO binding[26]. Developing catalytic materials with appropriate electronic properties becomes critical for tuning the interplay between these two criteria for selective C–C coupling.

Among all transition metals, Cu-based materials with unique electronic properties have been shown to be the most selective towards higher-value hydrocarbons beyond CO or HCOOH (refs [27,28]). Cu catalysts with different morphologies or structures present varied product distributions. Polished Cu polycrystalline foils with primarily (111) facets exposed can catalyse C–C coupling for C_{2+} products; however, these are not the major products, with Faradaic efficiencies usually much lower than those of C_1 products (HCOOH, CO, and CH_4)[27,29–31]. By pre-oxidizing Cu metal to oxide under high temperature in air and reducing it in situ to Cu again under CO_2 or CO reduction conditions, the C_{2+} selectivity was observed to be significantly improved[32–35]. However, the resulting Cu catalysts usually show complicated morphologies, which presents a challenge for mechanistic studies[32]. Electrocatalytic CO_2RR on single crystal Cu facets has suggested (100) surfaces to be more selective towards C_{2+} products than (111)[12,29,36–38], and further promoted by the introduction of steps on the (100) basal plane[10,12,28,39]. A deeper mechanistic understanding of C–C coupling on different Cu facets or atomic sites would provide valuable guidance for the design of catalysts for CO_2 reduction to C_{2+} products.

In this work, we first study the facet dependence of the initial C–C coupling steps on Cu in CO_2 reduction using density functional theory (DFT). Several recent studies have investigated C–C coupling using an implicit description of the ion distribution in the electrolyte[40–42]. Here, we apply an explicit model of the electrolyte to investigate solvation and cation stabilization of initial C–C coupling intermediates. Because simulations suggest both the Cu(100) and stepped facets to be more favourable for C_{2+} product formation over (111), we developed a metal ion cycling method to synthesize single crystalline Cu_2O nanocubes with predominantly Cu_2O(100) facets. By tuning the battery cycle numbers on the Cu foil, the product distributions and reaction pathways can be effectively controlled. Under CO_2RR conditions, those oxide nanocubes can be reduced to polycrystalline Cu nanocubes with preferentially exposed Cu(100) facets for C–C coupling. As a result, our 100-cycled Cu-nanocube catalyst presents a sixfold improvement in the C_{2+} to C_1 product ratio compared with the pristine polished Cu foil, with a C_{2+} Faradaic efficiency of over 60% and H_2 below 20%, and a corresponding C_{2+} partial current density of more than 40 mA cm^{-2}.

Results

DFT theoretical simulations. The mechanistic study of CO_2RR from ab initio simulations poses several major challenges—the

[1]Rowland Institute, Harvard University, Cambridge, MA, USA. [2]SUNCAT Center for Interface Science and Catalysis, Department of Chemical Engineering, Stanford University, Stanford, CA, USA. [3]Center for Nanoscale Systems, Harvard University, Cambridge, MA, USA. [4]Harvard John A. Paulson School of Engineering and Applied Sciences, Harvard University, Cambridge, MA, USA. [5]SUNCAT Center for Interface Science and Catalysis, SLAC National Accelerator Laboratory, Menlo Park, CA, USA. Kun Jiang and Robert B. Sandberg contributed equally to this work. *e-mail: chank@stanford.edu; hwang@rowland.harvard.edu

complexity of the reaction pathways towards the many products[43], the importance of electrochemical activation barriers[26], and the crucial role of cation and solvation stabilizations of reaction intermediates[44,45]. In electrochemical reactions involving H_2 or O_2 (hydrogen evolution reaction (HER), oxygen evolution reaction (OER), oxygen reduction reaction (ORR), hydrogen oxidation reaction (HOR)), thermodynamic criteria have been shown to be sufficient in describing activity and also in the prediction of new active catalysts[46–52]. However, in CO_2RR, activation energies for proton–electron transfer are crucial to the determination of activity even towards CH_4, the simplest hydrocarbon product[26]. CO_2RR intermediates with vertically oriented C–O bonds are also dramatically stabilized by the electric fields induced by cations and their image charges on the surface, which reach magnitudes of ~1 V Å^{-1} in the vicinity of the cations, as shown in Fig. 1a[44]. The determination of electrochemical transition states and the effect of cation promotion both require the explicit consideration of ions and solvating waters, which present many open questions from an atomistic modelling perspective[53–56].

Recently, CO dimerization has been found to be feasible on Cu in the presence of solvated cations. Cations are expected to be present at the interface when applied potentials are more negative than the potential of zero charge of Cu (approximately −0.7 V versus SHE (standard hydrogen electrode))[40,45,57], where CO_2RR occurs. A full kinetic analysis of the energetics of the complex pathways towards C_{2+} products and their facet dependence, especially with explicit consideration of ions and solvent layers and adsorbate–adsorbate interactions, would at present be computationally intractable. However, several observations suggest that a simple analysis of the steps towards *OCCHO may already provide some insights into C_{2+} activity on Cu. Firstly, a simple thermochemical analysis suggests the pathway from *OCCHO to ethanol or acetaldehyde to be thermodynamically downhill on Cu(211)[58]. Experimentally, glyoxal (OCHCHO) has been shown to be reduced to acetaldehyde and ethanol, which suggests it to be a critical intermediate in the formation of at least the oxygenated C_{2+} products[59,60]. Finally, a recent C_1 kinetic model[26] suggests the predominant species on Cu facets to be *CO and *H under CO reduction conditions, which suggests C_{2+} formation through a *CO dimerization process if the associated energetics are facile.

Here, we consider the energetics of *OCCO and *OCCHO formation on flat terraces of Cu, (100) and (111), and we consider (211) as a model facet for stepped sites. Firstly, to illustrate the effects of the interfacial electric field on the CO dimerization reaction, we show in Fig. 1b the binding free energies of 2*CO and *OCCO on these facets in vacuum as a function of an electric field applied along the *z*-direction perpendicular to the slab (Supplementary Fig. 1), with all energies given in Supplementary Table 1. Significant field-induced stabilizations are shown for both adsorbates on all facets, and the corresponding dipoles and polarizabilities of the adsorbates are given in Supplementary Table 2. Figure 1c shows free energy diagrams for the energetics of dimerization of *CO to form *OCCO and the subsequent surface hydrogenation or proton–electron transfer to form *OCCHO in the presence of explicit solvent. Proton–electron transfers at 0 V versus RHE and pH 7 are included in dashed lines, while surface hydrogenations through adsorbed *H are included as solid lines. The free energy diagram for the alternative pathway through CO–CHO coupling is shown in Supplementary Fig. 2. Additionally, free energy diagrams at −0.7 V versus RHE and pH 7 for these two pathways are shown in

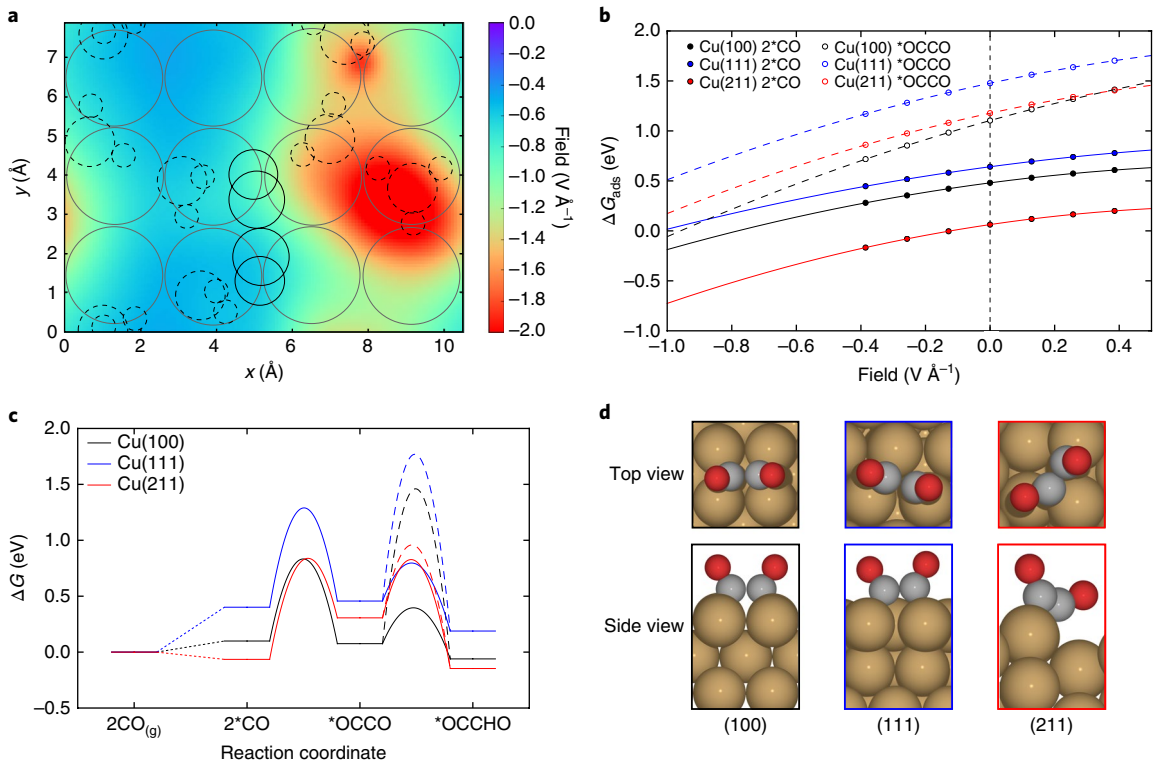

Fig. 1 | DFT simulations of C–C coupling on Cu facets. a, Contour plot of the electric field in the vicinity of an ion and its image charge on a Cu(100) surface. **b**, Binding free energies in vacuum for 2*CO and *OCCO as a function of electric field strength along the *z*-direction perpendicular to the slab. **c**, Free energy diagram at 0 V versus RHE (reversible hydrogen electrode) for the energetics of the dimerization of *CO to form *OCCO, and the subsequent surface hydrogenation (solid lines) and proton–electron transfer (dashed lines) to form *OCCHO in the presence of a solvent and cation-induced field. **d**, *OCCO configurations on the (100), (111) and (211) facets, where solvent molecules have been removed to show the adsorbate configurations.

Supplementary Figs. 3 and 4 to illustrate the effect of potential on the electrochemical steps. Free energy diagrams for the competitive hydrogen evolution reaction at 0 V and −0.7 V versus RHE are also included in Supplementary Figs. 5 and 6, respectively.

To provide the effect of cation-induced fields expected under reducing conditions, a simple hydronium ion is included in the solvent layer; similar fields were found for various alkali cations that are expected to be present[45,60], due to the lack of significant variations in ion–slab distances with ion size. Because the surface is negatively charged, we expect an excess of positive cations. An upper bound for anion concentrations would be 0.5%, corresponding to a standard bulk electrolyte concentration of 0.25 M. Anions and their image charges at the interface create fields in the opposite direction to that induced by cations. These fields would destabilize the intermediates through dipole–field interactions and not contribute to improving the CO_2 reduction rate. All associated energies, as well as the transfer coefficients for the proton–electron transfer steps, are given in Supplementary Tables 3–5.

At room temperature, the threshold for facile kinetics is approximately 0.75 eV, which corresponds to one turnover per second per site[61]. The free energy diagram suggests (100) to be significantly more facile for CO dimerization relative to (111). This result is consistent with experiments on single crystal Cu electrodes, where an earlier onset for C_2 products on (100) facets was observed[12,29]. *OCCO on (100) adsorbs on the fourfold site through its two carbon ends, which has a stronger intrinsic binding energy than on (111), where the carbon atoms are constrained to bind to a threefold site (see Fig. 1, panel b at zero field and panel d, and Supplementary Table 1). The dipole moment of the *OCCO on the (100) facet is also 0.2 eÅ higher than on (111) (Supplementary Table 2), which gives an additional stabilization in the presence of a cation-induced field, and is illustrated in Fig. 1b (for example, 0.2 eV in a -1 V Å^{-1} field). The subsequent proton–electron transfer to *OCCO to form *OCCHO has high barriers on both (100) and (111) facets, owing to the requirement that *OCCO rotate to orient the carbon end towards the solvent, similar to the rotational requirement of *CO to form *CHO (Supplementary Figs. 7–11). However, the corresponding surface hydrogenation to *OCCHO is surmountable and therefore not the limiting factor here.

Our calculations also suggest the stepped Cu(211) facet to show favourable CO dimerization kinetics. Although (211) has a larger dimerization barrier than (100), the energy of its transition state is essentially the same, which suggests a similar activity since *CO adsorption is facile (Supplementary Fig. 12). The surface hydrogenation to form *OCCHO is also facile, as is the corresponding proton–electron transfer barrier, since the carbon end of *OCCO is oriented towards the solvent for proton transfer (Supplementary Fig. 7). This result is also consistent with previous single-crystal data that showed increased C_2/C_1 selectivity on stepped facets compared with (111) facets[10].

A simple kinetic model of CO reduction towards CH_4 suggests a small *CHO coverage of up to ~10^{-6} on the (211) surface under CO reducing conditions[26], which has a more facile proton–electron transfer barrier to *CO than terraces (Supplementary Fig. 2). This *CHO may therefore also couple to *CO to form *OCCHO. This coupling barrier for all three facets is shown in Supplementary Fig. 2 and the associated energies are listed in Supplementary Table 4. These barriers are comparable to the dimerization barriers and are more likely to be competitive on the stepped (211) facet due to its relatively higher *CHO coverage.

Metal ion cycling of Cu_2O and Cu nanocubes. Our theoretical analysis suggests both (100) and stepped facets to have a significantly improved activity for C–C coupling compared with the (111) counterpart. In experiments, using bulk single crystals is straightforward and is also important for fundamental studies[12,29], but its large-scale deployment is limited by the small surface area and high cost. We therefore focus on preferentially exposing Cu(100) facets over (111) on polycrystalline Cu foils for selective C–C coupling in CO_2RR.

Here, our strategy is to controllably synthesize Cu_2O nanocubes with (100) facets onto Cu foil, which we show to retain a cubic structure when reduced to Cu metal with preferentially exposed Cu(100) facets due to the possible surface epitaxy[62,63]. We develop a Cu^{2+} ion cycling method (Fig. 2a and Methods), similar to a battery galvanostatic charging–discharging procedure (Fig. 2b), to modify the surface of Cu foil (Fig. 2c) into a uniform layer of single crystalline Cu_2O nanocubes (Fig. 2e). In contrast with traditional electrochemical deposition methods, the stripping–deposition cycling method gradually stabilizes a nanocube morphology and selectively exposes only the (100) facets[64]. This is confirmed by scanning electron microscopy (SEM) of Cu foils after 10 or 100 cycles (10-cycle Cu, 100-cycle Cu). The copper foil surface was first roughened after 10 galvanostatic cycles with trenches and tiny seeds (Fig. 2d), which after elongated cycles gradually evolve into cubic morphologies with very smooth (100) surfaces as shown in Fig. 2e, suggesting their single crystalline nature. As a result, the surface of the Cu foil is fully covered by Cu_2O nanocubes without preferentially oriented directions, consistent with the Raman spectra in Supplementary Fig. 13 and X-ray diffraction (XRD) pattern in Supplementary Fig. 14. More importantly, except for the roughened surfaces in Fig. 2f, the cubic structures were still maintained after Cu_2O was reduced in situ to Cu under CO_2RR conditions (Supplementary Fig. 15 and Methods), which could help to preferentially expose Cu (100) facets favourable for CO dimerization[62,63].

To further analyse the exposed facets of Cu_2O and Cu nanocubes, we used a focused ion beam (FIB) to cut ultra-thin specimens (~50 nm thick) for transmission electron microscopy (TEM) characterizations of cross-sections (Methods). The Cu_2O layer is less than 1 μm thick, with a few right angles observed due to the cubic structure. The selected area electron diffraction (SAED) pattern, performed in a relatively large spot of ~200 nm in diameter, further demonstrates the single crystallinity of each Cu_2O nanocube[65]. Due to the misalignment of the cube orientations during the FIB cutting process, the SAED zone axis is slightly deviated (~18.4°) from the [002] direction. In the aberration-corrected TEM image, the Cu_2O (200) atomic layers were identified with a spacing of ~2.03 Å, measured by integrating the pixel intensities over a few atomic layers, in agreement with the theoretical lattice parameter[66]. Polycrystalline Cu nanocubes were obtained after the prereduction process with observable pores formed, possibly due to the volume change (Fig. 3d). Cu_2O was fully reduced and no oxygen was detected by electron energy loss spectroscopy (EELS, Supplementary Fig. 16), eliminating possible effects from oxygen on CO_2RR catalysis. This is reinforced by the energy-dispersive X-ray mapping and spectra results shown in Supplementary Figs. 17 and 18. Although the SAED pattern in Fig. 3e shows the polycrystallinity of the Cu nanocubes, we observed a few brightest dots diffracted from a grain with [002] zone axis, suggesting that there is a significant portion of Cu (100) facets exposed in those nanocubes. This is further confirmed by TEM images where the Cu (200) square lattice was exposed, with a measured lattice spacing of 1.79 Å in Fig. 2f.

Electrocatalytic characterizations. The CO_2RR catalytic activities of polished Cu foil, 10-cycle Cu and 100-cycle Cu were tested in CO_2 saturated 0.25 M $KHCO_3$ aqueous electrolyte with a measured pH of 7.1 (Methods). The gas products were analysed by gas chromatography, and liquid products by nuclear magnetic resonance (NMR) spectroscopy (Supplementary Figs. 19 and 20, and Methods). Due to significantly increased surface roughness (Supplementary Figs. 21 and 22), the overall current densities of both 10- and 100-cycle Cu were dramatically increased compared with polished Cu foil (Fig. 4a).

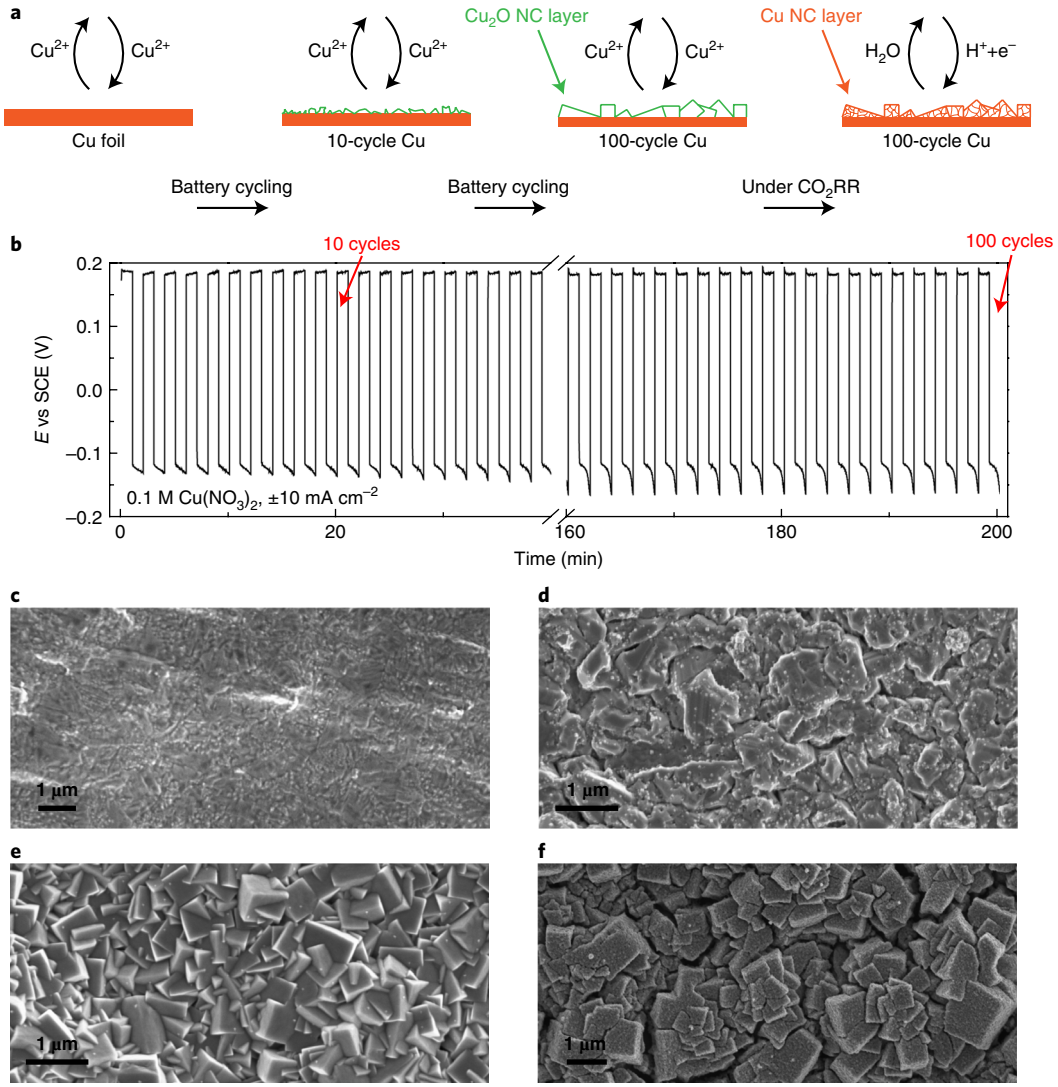

Fig. 2 | Cu^{2+} ion battery cycling of Cu_2O and Cu nanocubes. a, Schematic of the Cu^{2+} ion cycling method for Cu_2O and Cu nanocubes (NCs) on Cu foils. **b**, Galvanostatic cycling of Cu foil in 0.1 M $Cu(NO_3)_2$ solution with a fixed current density of 10 mA cm^{-2}. The 10-cycle Cu and 100-cycle Cu samples were stopped at the deposition status of the tenth and hundredth cycles, respectively. **c**–**e**, SEM images of the pristine Cu foil (**c**), 10-cycle Cu (**d**) and 100-cycle Cu (**e**). The 100-cycle Cu presents a surface covered by Cu_2O single crystalline nanocubes with smooth (100) facets. **f**, SEM image of 100-cycle Cu after the prereduction under CO_2RR conditions. Cu_2O nanocubes are reduced to Cu nanocubes with well-maintained cubic morphology. SCE, saturated calomel electrode.

The major CO_2RR products of polished Cu foil (Supplementary Fig. 23) are C_1 products including CO (32.1% Faradaic efficiency at −0.904 V versus RHE), HCOOH (48.3% Faradaic efficiency at −0.99 V versus RHE), and CH_4, which gradually increased at large overpotentials (34.7% Faradaic effiiency at −1.135 V versus RHE). C_{2+} products, including ethylene (C_2H_4), ethanol (EtOH), and *n*-propanol (*n*-P), were also observed with a highest Faradaic efficiency of 26.2%, smaller than C_1 products (58.6%). Although the current density of 10-cycle Cu was significantly boosted, the C_1 and C_{2+} product distribution did not show a significant enhancement from polished Cu. The highest C_{2+} selectivity is 22.3%, with a corresponding C_1 Faradaic efficiency of 47.9% (Supplementary Fig. 24). The C–C coupling selectivity was dramatically improved after 100 cycles of Cu foil with Cu nanocubes obtained (Fig. 4). C_2H_4 and EtOH emerged at an onset potential of −0.7 V versus RHE (Supplementary Table 6), and continued to increase with decreased C_1 products such as CO and HCOOH under more-negative potentials. C_2H_4 showed the highest selectivity in C_{2+} products, with a 32% Faradaic efficiency at −0.963 V versus RHE, where the C_{2+} Faradaic efficiency also reached its peak of 60.5%. This is approximately three times the selectivity of both C_1 (22.2%) and H_2 (20%). With a large overall current density of 68 mA cm^{-2} under that potential, the CO_2RR partial current reached 56 mA cm^{-2}, where 41 mA cm^{-2} came from C_{2+} products (Fig. 4e). This performance is among the best in existing literature (Supplementary Table 7). Compared with the pristine polished Cu foil and 10-cycle Cu, the 100-cycle catalyst with Cu nanocubes presents a sixfold improvement in C_{2+} to C_1 product ratio (Fig. 4f). This trend is consistent with theoretical simulations suggesting favourable CO-dimerization energetics on Cu(100) compared with (111) facets. Given the significantly increased roughness factor compared with polished foil, we also expect a potential increase in step sites, which are also suggested by theory to be favourable towards C–C coupling.

A critical measure for the catalytic stability of 100-cycle Cu is whether the cubic morphology can remain intact under long-term electrolysis. We monitored the gas products by automatic gas-chromatography sample injection every 20 min over the course of continuous electrolysis under −0.914 V versus RHE. Interestingly,

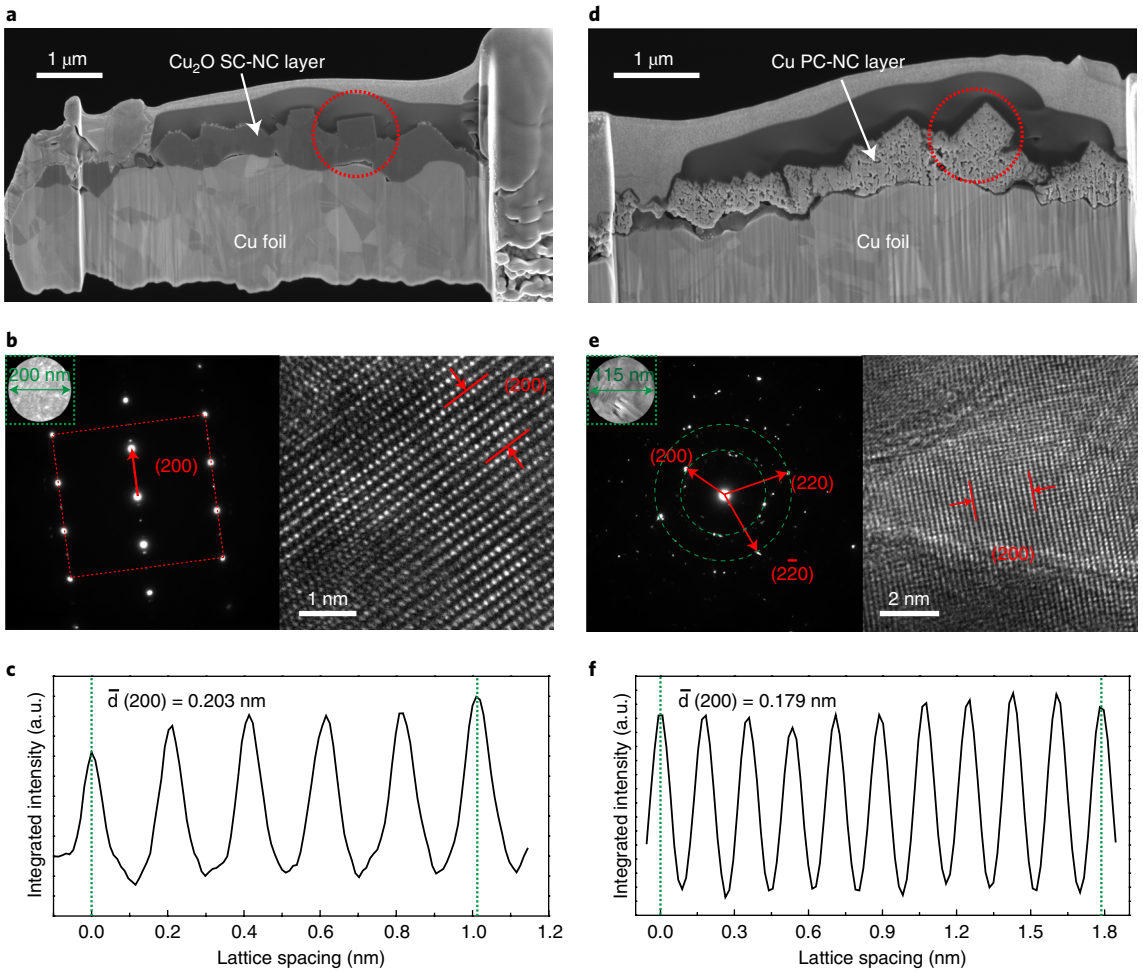

Fig. 3 | Cross-section FIB and TEM characterizations of Cu_2O and Cu nanocubes. a, SEM image of the Cu_2O nanocube cross-section cut by FIB. **b**, SAED pattern of the Cu_2O nanocube with an area of ~200 nm, suggesting its single crystallinity. The TEM image shows the (200) lattice. **c**, The lattice spacing measured by integrating a few atomic layers indicated in **b**. **d**, SEM image of the Cu nanocubes cross-section cut by FIB. **e**, SAED pattern of the Cu nanocube with an area of ~115 nm, suggesting its polycrystallinity. There are a few brightest diffraction dots with the same [002] zone axis, suggesting a significant portion of Cu(100) facets are exposed. The TEM image shows the (200) lattice. **f**, The lattice spacing measured by integrating a few atomic layers indicated in **e**. SC-NC, single crystalline-nanocube; PC-NC, polycrystalline-nanocube.

although the C_2H_4 Faradaic efficiency presents a slight decrease after two hours of electrolysis, the C_2H_4 partial current remains relatively stable at ~20 mA cm^{-2} due to compensation from gradually increased overall current (Supplementary Fig. 25). A careful post-catalysis SEM characterization reveals that the Cu cubic structure is well maintained, which may explain the stable C_2H_4 current. However, similar to previous studies[67], large (~5 μm) Cu particulate agglomerates are observed on the catalyst surface due to the high mobility of Cu atoms and the Cu ion dissolution and re-deposition processes, especially under large overpotentials and currents. These newly formed Cu particles contribute to the current increase, but mainly in C_1 and H_2 products due to the different facet exposed compared with our Cu nanocubes[67]. Future improvements to remove or prevent the large Cu particles by methods such as sonicating, recycling and surface coating can help to further extend the stability of Cu catalysts.

In our high-surface-area copper cubes, it is likely that the interfacial pH is higher relative to that on a polished Cu foil, because there is a higher OH^- production rate per geometric electrode area. We note, however, that our normalized activity data (Supplementary Fig. 22) suggests that, in addition to local pH effects, the intrinsic C_2 activity of these materials is superior to plain Cu foil. Drawing upon Hori's old analysis on CO reduction as a function of pH[68], an increase in pH at a given potential should suppress methane production, but keep C_2 activity constant. This observation is consistent with reports of improved C_2 versus C_1 selectivity as pH increases on Cu catalysts[10,69]. The origin of this pH effect is in the differences in the rate-determining steps between C_2 and C_1 products. Supplementary Fig. 22 shows that the intrinsic C_1 activity is indeed suppressed in the 100-cycle versus polished Cu, which may arise from an increased interfacial pH in the higher-surface-area 100-cycle catalyst. However, the intrinsic C_{2+} activity is enhanced, especially in the low-overpotential regions where transport effects are minimized. Based on Hori's extensive study of pH effects[68], this enhancement cannot be attributed to an increased interfacial pH, which suggests an increase in intrinsic C_{2+} activity in the catalysts, and is in accordance with our theoretical calculations pointing to the more facile coupling barriers on (100) and stepped facets.

Conclusion

The feedback loop between theory and experiment is increasingly important to advances in fundamental mechanistic understanding and catalyst discovery. Using a combined theoretical and experimental approach, we have developed an efficient Cu nanocube catalyst with significantly improved C_{2+} selectivity. The metal ion battery cycling method has been demonstrated to be effective in

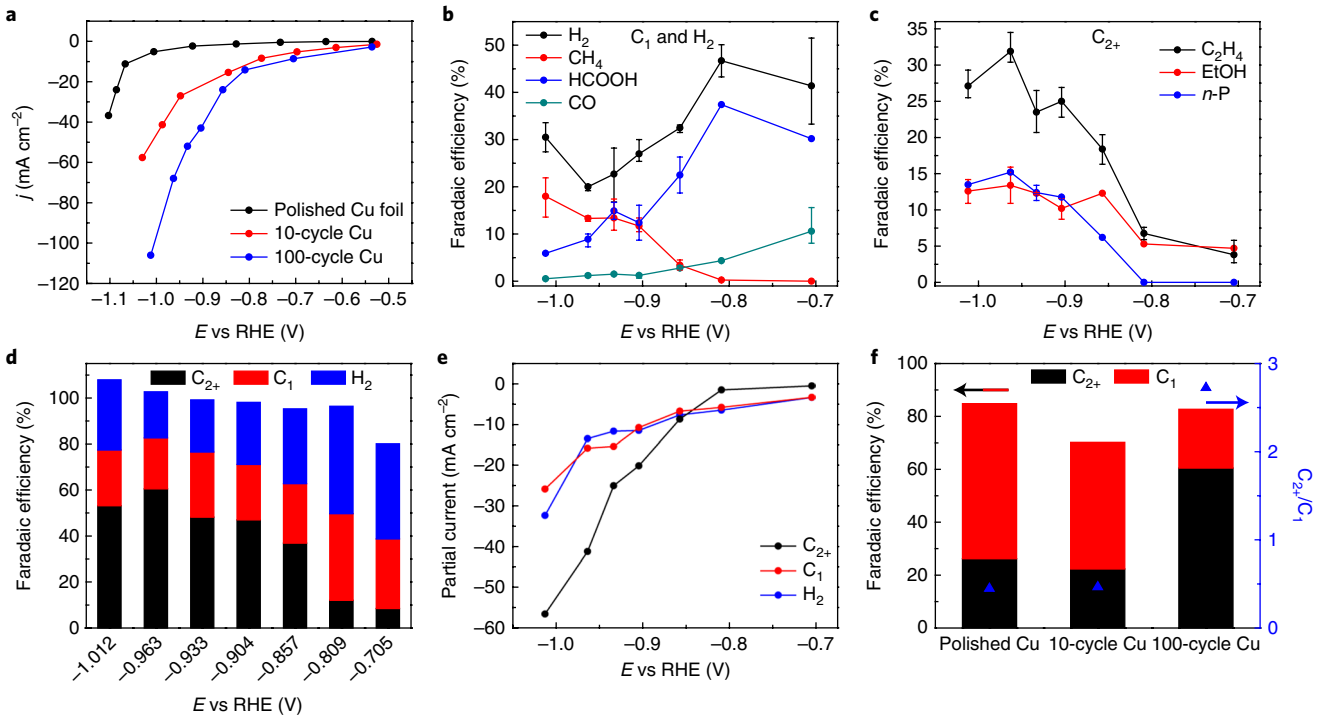

Fig. 4 | Electrocatalytic CO_2RR on polished Cu foil, 10-cycle Cu and 100-cycle Cu. a, The overall current densities of the three catalysts, where 100-cycle Cu shows a significantly increased current density compared with polished Cu foil. **b**,**c**, Faradaic efficiencies of each CO_2RR product on 100-cycle Cu under different potentials. The error bars represent three independent samples. **d**, Faradaic efficiencies of C_{2+}, C_1 and H_2 products on 100-cycle Cu under different potentials. The highest C_{2+} Faradaic efficiency reaches 60.5%. **e**, Partial currents of C_{2+}, C_1 and H_2 products of 100-cycle Cu. **f**, The highest C_{2+}/C_1 ratio of different catalysts. 100-cycle Cu exhibits a sixfold improvement compared with polished Cu foil.

controlling the surface morphology and facet exposure, by tuning the battery cycle numbers on Cu foils for desired reaction pathways and high-value C_{2+} products. This method can be further extended to other metal catalysts beyond Cu with a number of tuning knobs beyond the cycle numbers, including the concentration of metal ions, the charging–discharging current density and capacity, and the cycling temperature. Given the wide variety of metal catalysts and their corresponding catalytic reactions, the metal ion cycling method is promising for both fundamental mechanistic studies and technological applications in electrocatalysis. Further theoretical work will focus on kinetic modelling of C–C coupling on Cu, mass transport effects, trends among transition metals, and consideration of subsequent steps and alternate pathways.

Methods

Density functional theory calculations. Density functional theory (DFT) was used to calculate all reaction energetics. Geometry optimizations converged when force components were less than 0.05 eV Å^{-1}. Transition states were calculated using the climbing image nudged elastic band (NEB) method[70], with forces converged to 0.05 eV Å^{-1}. The BEEF-vdW exchange–correlation functional[71] and ultrasoft pseudopotentials were used with the Quantum Espresso code[72] within the Atomic Simulation Environment (ASE)[73]. A 500 eV plane–wave cutoff, 5,000 eV density cutoff, and a (4,4,1) *k*-point sampling were used for all calculations. To calculate free energies, a normal-mode analysis was performed on all species and the harmonic oscillator approximation was used[74]. Zero-point energies, entropic contributions and heat capacities were calculated based on the vibrations and used to correct the electronic energies[74].

To model the electrochemical interface, a 4×3×3 supercell of fcc Cu (100) and (111) was used with a single layer of either eight (for Cu(100)) or seven (for Cu(111)) water molecules at the surface. A 3×3×3 supercell with five water molecules was used for Cu(211). Water densities were chosen to be as close as possible to that of the Pt(111) bilayer structure found in ultrahigh-vacuum experiments within the unit cell sizes considered[75].

Water layer structures were initially determined using a minima-hopping algorithm, which alternates between molecular dynamics and geometry optimization steps to construct a series of local minima[76]. Geometry optimizations with the adsorbates were performed on all site types using the water structure found through minima hopping.

Because cation-induced fields lead to dramatic stabilizations of the adsorbates involved (Fig. 1b), an explicit cation is required in the simulations. We find that a simple hydronium ion gives similar fields to solvated alkali cations expected to be present under CO_2RR conditions[45,60]. A single hydrogen atom was therefore placed in the water layer. The ground-state electronic structure redistributes the charge from this atom's one electron to the metal, creating a charge-separated double layer[77].

A dipole correction in the *z*-direction was applied to explicit solvent calculations to compensate for the field resulting from the asymmetric slab in the vacuum region[78]. The potential-dependent electrochemical barriers were corrected based on the charge-extrapolation scheme[53]. All barriers were extrapolated to 4.0 eV, corresponding to 0 V_{RHE} at pH = 7, which are experimental conditions for CO_2 reduction. All transition states were referenced to aqueous protons and electrons, using the Computational Hydrogen Electrode[79]. Due to generalized gradient approximation functionals placing the unfilled CO $2\pi^*$ orbital too low in energy, an overbinding correction was applied to CO binding energies based on the vibrational frequency of the internal CO stretch of *CO, determined in vacuum[80,81]. These corrections were 0.28 eV for (100), 0.34 eV for (111) and 0.26 eV for (211).

We have focused on hydronium ions as proton sources, under the assumption that qualitative trends across facets and processes are still well described even if experimental conditions may favour a different proton source. From a computational perspective, anions at the interface are significantly more difficult to treat than cations due to band alignment of the solvent's highest occupied and lowest unoccupied molecular orbitals (HOMO/LUMO) and metal Fermi energy levels, which leads to artificial charge transfer. Further work will focus on development of methods to mitigate these fundamental challenges.

Electric field effects. For field calculations shown in Fig. 1b, a sawtooth potential was applied in the *z*-direction for structures of the adsorbates in vacuum, where the solvent layer was removed. The induced field was given by the slope of the electrostatic potential force as a function of distance, shown in Supplementary Fig. 1.

For calculation of the electric field strength at each coordinate in Fig. 1a, the adsorbate was removed and the following equation was used to calculate the field:

$$E = \frac{\mathrm{d}}{\mathrm{d}z}(V_{\mathrm{total}} - V_{\mathrm{slab}} - V_{\mathrm{water}} - V_{\mathrm{ion}}) \quad (1)$$

where E is the electric field strength, V_{total} is the total potential, V_{slab} is the slab potential, V_{water} is the water potential and V_{ion} is the ion potential from the hydronium ion.

The interaction energy between an adsorbate and an electric field at the interface is given by

$$\Delta E = \mu\varepsilon - \frac{1}{2}\alpha\varepsilon^2 + \ldots \quad (2)$$

where ΔE is the change in binding energy, ε is the electric field strength, and μ and α are the intrinsic dipole moment and polarizability of the adsorbate, respectively[61]. μ and α, found by fitting the curves in Fig. 1b to equation (1), are shown in Supplementary Table 2. Due to the larger difference in dipole moment between 2*CO and *OCCO on (100), the reaction energy on (100) becomes nearly thermoneutral at a field of -1 V Å^{-1}, while the reaction energies on (111) and (211) do not change considerably at these fields. The explicit water calculations with the hydronium ion give slight variations in energies compared to those obtained with a uniform field, which can be attributed to differences in solvation and fields at the adsorbate site, but exhibit the same trends. We note that the uncertainty in the energetics is increased by the presence of explicit solvent due to the additional degrees of freedom introduced by the water structure.

Reaction energetics. The reaction energetics for the CO–CO and CO–CHO coupling pathways to *OCCHO are shown in Fig. 1c of the main text and Supplementary Fig. 2, respectively. Additionally, reaction energetics for the hydrogen evolution reaction are shown in Supplementary Figs. 5 and 6. All of the binding energies used to construct the free energy diagrams are shown in Supplementary Table 3. Chemical barriers, consisting of coupling and surface hydrogenation, are shown in Supplementary Table 4, and electrochemical barriers, consisting of proton–electron transfers, are shown in Supplementary Table 5. Additionally, the associated transfer coefficients, β, for each proton–electron transfer reaction are shown (Supplementary Table 5). β represents the amount of charge transferred to the adsorbate at the transition state and scales the barrier as a function of potential[82]. All β values for *OCCO→*OCCHO were ~0.4, with slightly larger values for *CO→*CHO. The variation of the *OCCO protonation barrier on Cu(100) as a function of work function is shown in Supplementary Fig. 11 as an example.

Adsorbate geometries of proton–electron transfer to *OCCO to form *OCCHO. For the proton–electron transfer to *OCCO, the *OCCO configuration plays a crucial role, analogous to *CO protonation to *CHO in C_1 product formation, which was found to be significantly more facile on steps versus terraces[26]. Supplementary Fig. 6 shows the accessibility of the carbon end of *OCCO on a step site to accept a proton. *OCCO adsorbed on a step requires less rotation for proton transfer from the solvent than on a terrace, which rationalizes its lower barrier. *CO and *CHO configurations on (100), (111) and (211) are shown in Supplementary Figs. 8, 9 and 10, respectively.

Material preparation and characterization. All Cu foil (MTI Corp, 9 µm thickness, 99.99%) working electrodes were first cleaned by sonication in 0.5 M H_2SO_4 (prepared from 96% sulfuric acid, Sigma-Aldrich, ACS reagent grade). For the polished Cu foil samples, after rinsing with copious Milli-Q water (18.2 MΩ cm^{-1}), the Cu foils were electrochemically polished in phosphoric acid (Mallinckrodt Chemicals, 85% in water) by applying a voltage of +3 V versus graphite rod for 180 s.

For the synthesis of Cu_2O single crystalline nanocubes, the pre-cleaned Cu foil (1 cm^2) was chronopotentiometrically cycled in 0.1 M $Cu(NO_3)_2{\cdot}6H_2O$ (Alfa Aesar, 98%, deaerated with Ar) solution by applying an alternating current of ±10 mA (each for 1 min) versus another Cu foil (1 cm × 2 cm) counter electrode and a saturated calomel reference electrode (SCE, CH Instruments) for certain cycles.

The TEM, electron energy loss spectroscopy (EELS) and energy-dispersive X-ray spectroscopy (EDS) characterizations were carried out using a JEOL ARM200F aberration-corrected transmission electron microscope under 200 kV. Drift correction was applied during acquisition.

TEM sample preparation was performed using the standard liftout procedure with a dual-beam focused ion beam (FIB)-SEM equipped with a micromanipulator. An FEI 660 Helios Nanolab dual-beam, equipped with an OmniProbe 400 micromanipulator, was used to first deposit protective layers of carbon and platinum, and then to extract the specimen and mount it to a copper half-grid. Thinning was performed first at 30 kV, and then final polishing at 2 kV to remove amorphization and Ga implantation.

Powder X-ray diffraction data were collected using a Bruker D2 Phaser diffractometer in parallel beam geometry employing Cu Kα radiation and a one-dimensional LYNXEYE detector, at a scan speed of 0.02° per step and a holding time of 1 s per step. Raman spectroscopy was carried out on a WITEC CRM200 confocal Raman spectrometer with a 532 nm laser source and a typical dispersion grating of 600 g nm^{-1}.

Electrochemical measurements. All electrochemical measurements were run at 25 °C in a customized gastight H-type glass cell separated by Nafion 117 membrane (Fuel Cell Store). A BioLogic VMP3 work station was employed to record the electrochemical response. Certain amounts of $KHCO_3$ (Sigma-Aldrich, 99.95%) were dissolved in Milli-Q water to prepare the 0.25 M electrolyte, which was further purified by electrolysis between two graphite rods at 0.1 mA for 24 h to remove any trace amount of metal ions. In a typical three-electrode test system, a platinum foil (Beantown Chemical, 99.99%) and an SCE were used as the counter and reference electrode, respectively. All potentials measured against SCE were converted to the reversible hydrogen electrode (RHE) scale in this work using E (versus RHE) = E (versus SCE) + 0.244 V + 0.0591 × pH, where pH values of electrolytes were determined by an Orion 320 PerpHecT LogR Meter (Thermo Scientific). Solution resistance (R_u) was determined by potentiostatic electrochemical impedance spectroscopy (PEIS) at frequencies ranging from 0.1 Hz to 200 kHz, and manually compensated as E (iR corrected versus RHE, where iR is the voltage drop from electrolyte resistance) = E (versus RHE) − $R_u \times I$ (amps of average current). The prereduction was performed by holding −1.2 V versus SCE potential on the working electrode in CO_2-saturated electrolyte until the current remains stable.

CO_2 reduction products analysis. During electrolysis, CO_2 gas (Airgas, 99.995%) was delivered into the cathodic compartment containing CO_2-saturated electrolyte (20 ml, stirring at 600 r.p.m.) at a rate of 50.0 standard cubic centimetres per minute (sccm, monitored by Alicat Scientific mass flow controller) and vented into a gas chromatograph (Shimadzu GC-2014) equipped with a combination of molecular sieve 5 A, Hayesep Q, Hayesep T, and Hayesep N columns. A thermal conductivity detector (TCD) was mainly used to quantify H_2 concentration, and a flame ionization detector (FID) with a methanizer was used for a quantitative analysis of CO and other alkane contents. The detectors are calibrated by two independent standard gases from Airgas (containing 1,042 ppm of H_2 and 496.7 ppm of CO) and Scott Gas (containing 100 ppm of H_2, 100 ppm of CO, 100 ppm of CH_4, 101 ppm of C_2H_4 and 100 ppm of C_2H_6). The gas products were sampled after a continuous electrolysis of ~20 min under each potential. The partial current density for a given gas product was calculated as below:

$$j_i = x_i \times v \times \frac{n_i F p_0}{RT} \times (\text{electrode area})^{-1} \quad (3)$$

where x_i is the volume fraction of certain product determined by online gas chromatography referenced to calibration curves from the above two standard gas samples, v is the flow rate of 50.0 sccm, n_i is the number of electrons transferred, $p_0 = 101.3$ kPa, F is the Faradaic constant and R is the gas constant. The corresponding Faradaic efficiency at each potential is calculated by $FE = j_i / i_{total} \times 100\%$.

1D ^{1}H NMR spectra were collected on an Agilent DD2 600 MHz spectrometer with a water suppression technique to quantify the liquid products. Typically, 600 µl of electrolyte after electrolysis was mixed with 100 µl of D_2O (Sigma-Aldrich, 99.9 atom % deuterium) and 0.05 µl dimethyl sulfoxide (DMSO, Sigma-Aldrich, 99.9%), the internal standard. Typically, the peaks at ~8.3 ppm for $HCOO^-$, ~3.5 ppm for C_3H_7OH and ~1.0 ppm for C_2H_5OH were integrated, and the ratios of identified product peak area to DMSO peak (~2.6 ppm) area were compared to standard curves to quantify the concentrations of certain CO_2 reduction products, respectively. The error range is usually within approximately ±5%.

Data availability. The data that support the findings of this study are available from the corresponding authors upon reasonable request.

Received: 22 June 2017; Accepted: 17 November 2017;
Published online: 15 January 2018

References

1. Obama, B. The irreversible momentum of clean energy. *Science* **355**, 126–129 (2017).
2. Chu, S., Cui, Y. & Liu, N. The path towards sustainable energy. *Nat. Mater.* **16**, 16–22 (2017).
3. Lewis, N. S. Research opportunities to advance solar energy utilization. *Science* **351**, aad1920 (2016).
4. Liu, C., Colón, B. C., Ziesack, M., Silver, P. A. & Nocera, D. G. Water splitting–biosynthetic system with CO_2 reduction efficiencies exceeding photosynthesis. *Science* **352**, 1210–1213 (2016).
5. Cook, T. R. et al. Solar energy supply and storage for the legacy and nonlegacy worlds. *Chem. Rev.* **110**, 6474–6502 (2010).
6. Concepcion, J. J., House, R. L., Papanikolas, J. M. & Meyer, T. J. Chemical approaches to artificial photosynthesis. *Proc. Natl Acad. Sci. USA* **109**, 15560–15564 (2012).
7. Lewis, N. S. & Nocera, D. G. Powering the planet: chemical challenges in solar energy utilization. *Proc. Natl Acad. Sci. USA* **103**, 15729–15735 (2006).
8. Sakimoto, K. K., Wong, A. B. & Yang, P. Self-photosensitization of nonphotosynthetic bacteria for solar-to-chemical production. *Science* **351**, 74–77 (2016).

9. Rosen, B. A. et al. Ionic liquid-mediated selective conversion of CO_2 to CO at low overpotentials. *Science* **334**, 643–644 (2011).
10. Hori, Y. in *Modern Aspects of Electrochemistry Modern Aspects of* Electrochemistry (eds Vayenas, C. G., White, R. E. & Gamboa-Aldeco, M. E.) 89–189 (Springer, New York, 2008).
11. Zhu, D. D., Liu, J. L. & Qiao, S. Z. Recent advances in inorganic heterogeneous electrocatalysts for reduction of carbon dioxide. *Adv. Mater.* **28**, 3423–3452 (2016).
12. Hori, Y., Takahashi, I., Koga, O. & Hoshi, N. Selective formation of C_2 compounds from electrochemical reduction of CO_2 at a series of copper single crystal electrodes. *J. Phys. Chem. B* **106**, 15–17 (2002).
13. Jiang, K. *et al.* Transition-metal single atoms in a graphene shell as active centers for highly efficient artificial photosynthesis. *Chem* https://doi.org/10.1016/j.chempr.2017.09.014 (2017).
14. Liu, M. et al. Enhanced electrocatalytic CO_2 reduction via field-induced reagent concentration. *Nature* **537**, 382–386 (2016).
15. Saberi Safaei, T. et al. High-density nanosharp microstructures enable efficient CO_2 electroreduction. *Nano Lett.* **16**, 7224–7228 (2016).
16. Gao, S. et al. Partially oxidized atomic cobalt layers for carbon dioxide electroreduction to liquid fuel. *Nature* **529**, 68–71 (2016).
17. Chen, Y., Li, C. W. & Kanan, M. W. Aqueous CO_2 reduction at very low overpotential on oxide-derived Au nanoparticles. *J. Am. Chem. Soc.* **134**, 19969–19972 (2012).
18. Lin, S. et al. Covalent organic frameworks comprising cobalt porphyrins for catalytic CO_2 reduction in water. *Science* **349**, 1208–1213 (2015).
19. Kornienko, N. et al. Metal–organic frameworks for electrocatalytic reduction of carbon dioxide. *J. Am. Chem. Soc.* **137**, 14129–14135 (2015).
20. Zhang, S. et al. Polyethylenimine-enhanced electrocatalytic reduction of CO_2 to formate at nitrogen-doped carbon nanomaterials. *J. Am. Chem. Soc.* **136**, 7845–7848 (2014).
21. Zhang, S., Kang, P. & Meyer, T. J. Nanostructured tin catalysts for selective electrochemical reduction of carbon dioxide to formate. *J. Am. Chem. Soc.* **136**, 1734–1737 (2014).
22. Lei, F. et al. Metallic tin quantum sheets confined in graphene toward high-efficiency carbon dioxide electroreduction. *Nat. Commun.* **7**, 12697 (2016).
23. Sharma, P. P. et al. Nitrogen-doped carbon nanotube arrays for high-efficiency electrochemical reduction of CO_2: on the understanding of defects, defect density, and selectivity. *Angew. Chem. Int. Ed.* **127**, 13905–13909 (2015).
24. Zhang, X. et al. Highly selective and active CO_2 reduction electrocatalysts based on cobalt phthalocyanine/carbon nanotube hybrid structures. *Nat. Commun.* **8**, 14675 (2017).
25. Verma, S., Kim, B., Jhong, H.-R. M., Ma, S. & Kenis, P. J. A. A gross-margin model for defining technoeconomic benchmarks in the electroreduction of CO_2. *ChemSusChem* **9**, 1972–1979 (2016).
26. Liu, X. et al. Understanding trends in CO_2 reduction on transition metals. *Nat. Commun.* **8**, 15438 (2017).
27. Kuhl, K. P., Cave, E. R., Abram, D. N. & Jaramillo, T. F. New insights into the electrochemical reduction of carbon dioxide on metallic copper surfaces. *Energy Environ. Sci.* **5**, 7050–7059 (2012).
28. Hori, Y., Takahashi, I., Koga, O. & Hoshi, N. Electrochemical reduction of carbon dioxide at various series of copper single crystal electrodes. *J. Mol. Catal. A Chem.* **199**, 39–47 (2003).
29. Schouten, K. J. P., Qin, Z., Gallent, E. P. & Koper, M. T. M. Two pathways for the formation of ethylene in CO reduction on single-crystal copper electrodes. *J. Am. Chem. Soc.* **134**, 9864–9867 (2012).
30. Calle-Vallejo, F. & Koper, M. T. M. Theoretical considerations on the electroreduction of CO to C_2 species on Cu(100) electrodes. *Angew. Chem. Int. Ed.* **52**, 7282–7285 (2013).
31. Xie, M. S. et al. Amino acid modified copper electrodes for the enhanced selective electroreduction of carbon dioxide towards hydrocarbons. *Energy Environ. Sci.* **9**, 1687–1695 (2016).
32. Li, C. W. & Kanan, M. W. CO_2 reduction at low overpotential on cu electrodes resulting from the reduction of thick Cu_2O films. *J. Am. Chem. Soc.* **134**, 7231–7234 (2012).
33. Li, C. W., Ciston, J. & Kanan, M. W. Electroreduction of carbon monoxide to liquid fuel on oxide-derived nanocrystalline copper. *Nature* **508**, 504–507 (2014).
34. Ma, M., Djanashvili, K. & Smith, W. A. Controllable hydrocarbon formation from the electrochemical reduction of CO_2 over Cu nanowire arrays. *Angew. Chem. Int. Ed.* **128**, 6792–6796 (2016).
35. Mistry, H. et al. Highly selective plasma-activated copper catalysts for carbon dioxide reduction to ethylene. *Nat. Commun.* **7**, 12123 (2016).
36. Huang, Y., Handoko, A. D., Hirunsit, P. & Yeo, B. S. Electrochemical reduction of CO_2 using copper single-crystal surfaces: effects of CO* coverage on the selective formation of ethylene. *ACS Catal.* **7**, 1749–1756 (2017).
37. Roberts, F. S., Kuhl, K. P. & Nilsson, A. High selectivity for ethylene from carbon dioxide reduction over copper nanocube electrocatalysts. *Angew. Chem. Int. Ed.* **54**, 5179–5182 (2015).
38. Roberts, F. S., Kuhl, K. P. & Nilsson, A. Electroreduction of carbon monoxide over a copper nanocube catalyst: surface structure and pH dependence on selectivity. *ChemCatChem* **8**, 1119–1124 (2016).
39. Loiudice, A. et al. Tailoring copper nanocrystals towards C_2 products in electrochemical CO_2 reduction. *Angew. Chem. Int. Ed.* **55**, 5789–5792 (2016).
40. Goodpaster, J. D., Bell, A. T. & Head-Gordon, M. Identification of possible pathways for C–C bond formation during electrochemical reduction of CO_2: new theoretical insights from an improved electrochemical model. *J. Phys. Chem. Lett.* **7**, 1471–1477 (2016).
41. Xiao, H., Cheng, T., Goddard, W. A. & Sundararaman, R. Mechanistic explanation of the pH dependence and onset potentials for hydrocarbon products from electrochemical reduction of CO on Cu (111). *J. Am. Chem. Soc.* **138**, 483–486 (2016).
42. Xiao, H., Cheng, T. & Goddard, W. A. Atomistic mechanisms underlying selectivities in C_1 and C_2 products from electrochemical reduction of CO on Cu(111). *J. Am. Chem. Soc.* **139**, 130–136 (2017).
43. Kortlever, R., Shen, J., Schouten, K. J. P., Calle-Vallejo, F. & Koper, M. T. M. Catalysts and reaction pathways for the electrochemical reduction of carbon dioxide. *J. Phys. Chem. Lett.* **6**, 4073–4082 (2015).
44. Chen, L. D., Urushihara, M., Chan, K. & Nørskov, J. Electric field effects in electrochemical CO_2 reduction. *ACS Catal.* **6**, 7133–7139 (2016).
45. Montoya, J. H., Shi, C., Chan, K. & Norskov, J. K. Theoretical insights into a CO dimerization mechanism in CO_2 electroreduction. *J. Phys. Chem. Lett.* **6**, 2032–2037 (2015).
46. Hinnemann, B. et al. Biomimetic hydrogen evolution: MoS_2 nanoparticles as catalyst for hydrogen evolution. *J. Am. Chem. Soc.* **127**, 5308–5309 (2005).
47. Kibsgaard, J. et al. Designing an improved transition metal phosphide catalyst for hydrogen evolution using experimental and theoretical trends. *Energy Environ. Sci.* **8**, 3022–3029 (2015).
48. Zheng, Y., Jiao, Y., Jaroniec, M. & Qiao, S. Z. Advancing the electrochemistry of the hydrogen-evolution reaction through combining experiment and theory. *Angew. Chem. Int. Ed.* **54**, 52–65 (2015).
49. Greeley, J., Jaramillo, T. F., Bonde, J., Chorkendorff, I. & Norskov, J. K. Computational high-throughput screening of electrocatalytic materials for hydrogen evolution. *Nat. Mater.* **5**, 909–913 (2006).
50. Zhang, J., Zhao, Z., Xia, Z. & Dai, L. A metal-free bifunctional electrocatalyst for oxygen reduction and oxygen evolution reactions. *Nat. Nanotech.* **10**, 444–452 (2015).
51. Seitz, L. C. et al. A highly active and stable $IrO_x/SrIrO_3$ catalyst for the oxygen evolution reaction. *Science* **353**, 1011–1014 (2016).
52. Wang, H. et al. Direct and continuous strain control of catalysts with tunable battery electrode materials. *Science* **354**, 1031–1036 (2016).
53. Chan, K. & Nørskov, J. K. Electrochemical barriers made simple. *J. Phys. Chem. Lett.* **6**, 2663–2668 (2015).
54. Schnur, S. & Groß, A. Challenges in the first-principles description of reactions in electrocatalysis. *Catal. Today* **165**, 129–137 (2011).
55. Hormann, N. G. et al. Some challenges in the first-principles modeling of structures and processes in electrochemical energy storage and transfer. *J. Power Sources* **275**, 531–538 (2015).
56. Calle-Vallejo, F. & Koper, M. T. M. First-principles computational electrochemistry: achievements and challenges. *Electrochim. Acta* **84**, 3–11 (2012).
57. Sandberg, R., Montoya, J. H., Chan, K. & Norskov, J. CO–CO coupling on Cu facets: strain and coverage effects. *Surf. Sci.* **654**, 56–62 (2016).
58. Bertheussen, E. et al. Acetaldehyde as an intermediate in the electroreduction of carbon monoxide to ethanol on oxide-derived copper. *Angew. Chem. Int. Ed.* **55**, 1450–1454 (2016).
59. Schouten, K. J. P., Kwon, Y., Ham, C. J. Mvd, Qin, Z. & Koper, M. T. M. A new mechanism for the selectivity to C_1 and C_2 species in the electrochemical reduction of carbon dioxide on copper electrodes. *Chem. Sci.* **2**, 1902–1909 (2011).
60. Resasco, J. et al. Promoter effects of alkali metal cations on the electrochemical reduction of carbon dioxide. *J. Am. Chem. Soc.* **139**, 11277–11287 (2017).
61. Norskov, J. K., Studt, F., Abild-Pedersen, F. & Bligaard, T. *Fundamental Concepts in Heterogeneous Catalysis* (Wiley, Hoboken, NJ, 2014).
62. Ikemiya, N., Kubo, T. & Hara, S. In situ AFM observations of oxide film formation o n Cu(111) and Cu (100) surfaces under aqueous alkaline solutions. *Surf. Sci.* **323**, 81–90 (1995).
63. Zhou, G. & Yang, J. C. Formation of quasi-one-dimensional Cu_2O structures by in situ oxidation of Cu(100). *Phys. Rev. Lett.* **89**, 106101 (2002).
64. Shang, Y. & Guo, L. Facet-controlled synthetic strategy of Cu_2O-based crystals for catalysis and sensing. *Adv. Sci.* **2**, 1500140 (2015).
65. Huang, W.-C., Lyu, L.-M., Yang, Y.-C. & Huang, M. H. Synthesis of Cu_2O nanocrystals from cubic to rhombic dodecahedral structures and their comparative photocatalytic activity. *J. Am. Chem. Soc.* **134**, 1261–1267 (2012).
66. Oba, F. et al. Epitaxial growth of cuprous oxide electrodeposited onto semiconductor and metal substrates. *J. Am. Chem. Soc.* **88**, 253–270 (2005).

67. Manthiram, K., Beberwyck, B. J. & Alivisatos, A. P. Enhanced electrochemical methanation of carbon dioxide with a dispersible nanoscale copper catalyst. *J. Am. Chem. Soc.* **136**, 13319–13325 (2014).
68. Hori, Y., Takahashi, R., Yoshinami, Y. & Murata, A. Electrochemical reduction of CO at a copper electrode. *J. Phys. Chem. B* **101**, 7075–7081 (1997).
69. Kas, R., Kortlever, R., Yılmaz, H., Koper, M. T. M. & Mul, G. Manipulating the hydrocarbon selectivity of copper nanoparticles in CO_2 electroreduction by process conditions. *ChemElectroChem* **2**, 354–358 (2015).
70. Henkelman, G., Uberuaga, B. P. & Jonsson, H. A climbing image nudged elastic band method for finding saddle points and minimum energy paths. *J. Chem. Phys.* **113**, 9901–9904 (2000).
71. Wellendorff, J. et al. Density functionals for surface science: exchange-correlation model development with Bayesian error estimation. *Phys. Rev. B* **85**, 235149 (2012).
72. Giannozzi, P. et al. QUANTUM ESPRESSO: a modular and open-source software project for quantum simulations of materials. *J. Phys. Condens. Matter* **21**, 395502 (2009).
73. Bahn, S. R. & Jacobsen, K. W. An object-oriented scripting interface to a legacy electronic structure code. *Comput. Sci. Eng.* **4**, 56–66 (2002).
74. Cramer, C. J. *Essentials of Computational Chemistry* (Wiley, Chichester, 2004).
75. Ogasawara, H. et al. Structure and bonding of water on Pt(111). *Phys. Rev. Lett.* **89**, 276102 (2002).
76. Goedecker, S. Minima hopping: an efficient search method for the global minimum of the potential energy surface of complex molecular systems. *J. Chem. Phys.* **120**, 9911–9917 (2004).
77. Rossmeisl, J., Skulason, E., Bjorketun, M. E., Tripkovic, V. & Norskov, J. K. Modeling the electrified solid–liquid interface. *Chem. Phys. Lett.* **466**, 68–71 (2008).
78. Bengtsson, L. Dipole correction for surface supercell calculations. *Phys. Rev. B* **59**, 12301–12304 (1999).
79. Norskov, J. K. et al. Origin of the overpotential for oxygen reduction at a fuel-cell cathode. *J. Phys. Chem. B* **108**, 17886–17892 (2004).
80. Abild-Pedersen, F. & Andersson, M. P. CO adsorption energies on metals with correction for high coordination adsorption sites: a density functional study. *Surf. Sci.* **601**, 1747–1753 (2007).
81. Mason, S. E., Grinberg, I. & Rappe, A. M. First-principles extrapolation method for accurate CO adsorption energies on metal surfaces. *Phys. Rev. B* **69**, 161401 (2004).
82. Chan, K. & Nørskov, J. K. Potential dependence of electrochemical barriers from ab initio calculations. *J. Phys. Chem. Lett.* **7**, 1686–1690 (2016).

Acknowledgements

This work was supported by the Rowland Fellows Program at Rowland Institute, Harvard University. H.W. and K.J. acknowledge great support from C. M. Friend at Harvard University. This work was performed in part at the Center for Nanoscale Systems (CNS), a member of the National Nanotechnology Infrastructure Network (NNIN), which is supported by the National Science Foundation under NSF award no. ECS-0335765. CNS is part of Harvard University. Theoretical calculations were based upon work performed by the Joint Center for Artificial Photosynthesis, a DOE Energy Innovation Hub, supported through the Office of Science of the US Department of Energy under award no. DE-SC0004993. This research used resources of the National Energy Research Scientific Computing Center, a DOE Office of Science User Facility supported by the Office of Science of the US Department of Energy under contract no. DE-AC02-05CH11231.

Author contributions

H.W. designed the experiments of this project. K.C. designed the simulations of this project. K.J. and H.W. performed materials synthesis and catalysis measurements. K.J., A.J.A. and H.W. performed material characterizations. R.B.S., X.L. and K.C. performed simulations. H.W., K.J., K.C., R.B.S. and X.L. wrote the manuscript. K.J., R.B.S., A.J.A., X.L., D.C.B., J.K.N., K.C. and H.W. analysed the results.

Competing interests

The authors declare no competing financial interests.

Additional information

Supplementary information is available for this paper at https://doi.org/10.1038/s41929-017-0009-x.

Reprints and permissions information is available at www.nature.com/reprints.

Correspondence and requests for materials should be addressed to K.C. or H.W.

Publisher's note: Springer Nature remains neutral with regard to jurisdictional claims in published maps and institutional affiliations.